WEP Warwick Evans Publishing

Transactions on Computer Science and Intelligent Systems Research
ISSN: 2960-1800, eISSN: 2960-2238 | Volume 11
TPCEE 2025

Advancing Analytic Halo Mass Function Models Through Large-Scale Cosmological Simulations

Jiaye Miao

Saint Andrew's School, Boca Raton, USA

jiaye.miao@saintandrews.net

Abstract. We develop an analytic halo mass function (HMF) framework calibrated on the comprehensive Abacus-Summit simulations, achieving 2–3% accuracy for ΛCDM ($\lesssim$5% for extended cosmologies with massive neutrinos, evolving dark energy, and modified power spectra) across 10^{11}--$10^{15}M_{\odot}$ and 0<z<3. Unlike universal forms limited to ΛCDM, our MCMC-optimized model explicitly incorporates redshift and cosmology dependence while maintaining physical interpretability. The analytic formulation enables application to new physics without costly retraining, complementing more precise but less flexible emulator-based approaches. We quantify systematic uncertainties from resolution effects, sample variance, and mass definitions, and outline future improvements through symbolic regression. This work provides a robust tool for cosmological tests with galaxy clusters and large-scale structure at percent-level precision.

Keywords: Cosmology; Dark Matter; Galaxy Cluster; Halo Mass Function; Analytic modeling.

1. Introduction

The Λ Cold Dark Matter (ΛCDM) paradigm, the standard model of modern cosmology [1], describes a universe composed of ~70% dark energy (Λ), ~25% dark matter, and ~5% baryonic matter. This framework successfully explains observations of the Cosmic Microwave Background (CMB), the relic radiation from the early universe. Key missions including COBE [2], WMAP [3], and *Planck* have progressively mapped CMB anisotropies, refining cosmological parameters and strongly supporting ΛCDM, with *Planck* providing the highest-resolution full-sky CMB map to date.

1.1. Tension in cosmology

The ΛCDM model faces several observational tensions, most notably in the Hubble constant H_0. While *Planck* CMB measurements yield $H_0 = 67.0 \pm 0.6$ km/s/Mpc [4], local distance-ladder measurements from SH0ES give $H_0 = 73.04 \pm 1.04$ km/s/Mpc [5], a $\sim 3\sigma$ discrepancy. Similarly, DESI's BAO measurements show a 2.3σ tension with ΛCDM, favoring dynamical dark energy at 3.1σ when combined with CMB data [6]. The S_8 parameter, measuring matter clustering, also shows tension, with weak lensing surveys like KiDS [7] and DES [8] consistently reporting lower values than *Planck*'s $S_8 = 0.834 \pm 0.016$.

While recent analyses have reduced some tensions [9], these discrepancies highlight the need for independent cosmological probes. The persistent H_0 and S_8 tensions, along with DESI's preference for evolving dark energy, motivate rigorous testing of ΛCDM through complementary observations. Cross-validation across CMB, supernovae, weak lensing, and other methods remains crucial to distinguish between systematic effects and potential new physics beyond the standard cosmological model.

1.2. Cosmology via galaxy clusters

Galaxy clusters, the most massive bound structures in the Universe, serve as powerful cosmological probes through their abundance and mass distribution [10, 11]. Their formation traces the growth of cosmic structure, making the cluster mass function sensitive to key parameters like Ω_m, σ_8, and dark energy properties [12]. Cluster masses can be measured via weak lensing (direct total mass estimates)

[13], X-ray observations (hydrostatic equilibrium of hot gas) [14], and the Sunyaev-Zel'dovich effect (redshift-independent CMB distortion) [15], with each method providing complementary constraints on cosmological parameters.

Next-generation surveys will revolutionize cluster cosmology through unprecedented precision. Facilities like Rubin Observatory, Euclid, and Roman will improve photometric detection, while DESI, PFS, and WEAVE enhance spectroscopic follow-up. Combined with X-ray missions and CMB experiments (Simons Observatory, LiteBIRD), these will achieve percent-level constraints on cosmological parameters, complementing CMB and large-scale structure results.

First Rubin Observatory LSST image showing the Virgo Cluster and $\sim 10^7$ galaxies in a 3200 MP exposure (2% of full field)

Gravitational lensing by a massive cluster (Hubble)

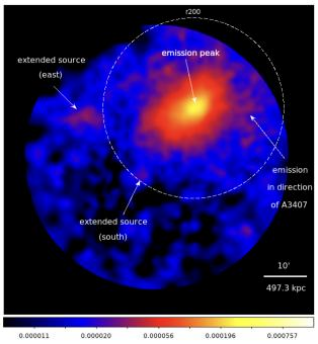

eROSITA X-ray map of galaxy cluster showing hot ICM

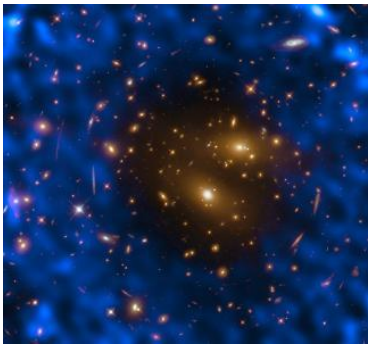

Optical-SZ composite of galaxy cluster showing CMB distortion

Figure 1. Multi-wavelength galaxy cluster views: (a) Rubin optical image of Virgo cluster; (b) Hubble's strong-lensing view of Abell 370; (c) eROSITA X-ray map of hot gas; (d) ALMA SZ effect on RX J1347.5–1145 with optical overlay

1.3. Halo mass function

The Halo Mass Function (HMF) quantifies the abundance of dark matter halos as a function of mass and redshift, serving as a critical link between primordial density fluctuations and observed large-scale structure. The HMF's dependence on cosmological parameters (Ω_{m}, σ_8, neutrino mass, and dark energy equation of state) makes it a powerful probe for testing models of structure formation [12, 16], with precise measurements enabling stringent constraints on both standard ΛCDM and its extensions.

Achieving $\sim 1\%$ HMF accuracy across $10^{11}-10^{15}M_{\odot}$ and $0<z<3$ is essential for next-generation surveys like Rubin LSST and Euclid [17, 18]. Such precision is particularly crucial for distinguishing subtle effects of massive neutrinos, dynamical dark energy, or modified gravity from ΛCDM predictions [19], ensuring unbiased cosmological constraints in the precision era.

1.4. Simulation-based modeling

Traditional HMF modeling relies on analytic approximations calibrated to limited Λ CDM simulations, restricting applicability to standard cosmologies. While cosmological N-body simulations provide more accurate nonlinear structure formation predictions [20, 21], their computational cost has historically limited parameter space coverage, particularly for extensions like massive neutrinos or modified gravity.

Modern simulation suites (Mira-Titan, Quijote, Abacus-Summit) now enable Gpc^3-scale modeling with $\sim 10^9 M_{\odot}$ resolution, supporting machine learning emulators for HMF prediction. However, these emulators [22, 23] face challenges when extrapolating beyond their training domains, particularly for non-standard cosmologies, leaving residual uncertainties in small-scale physics.

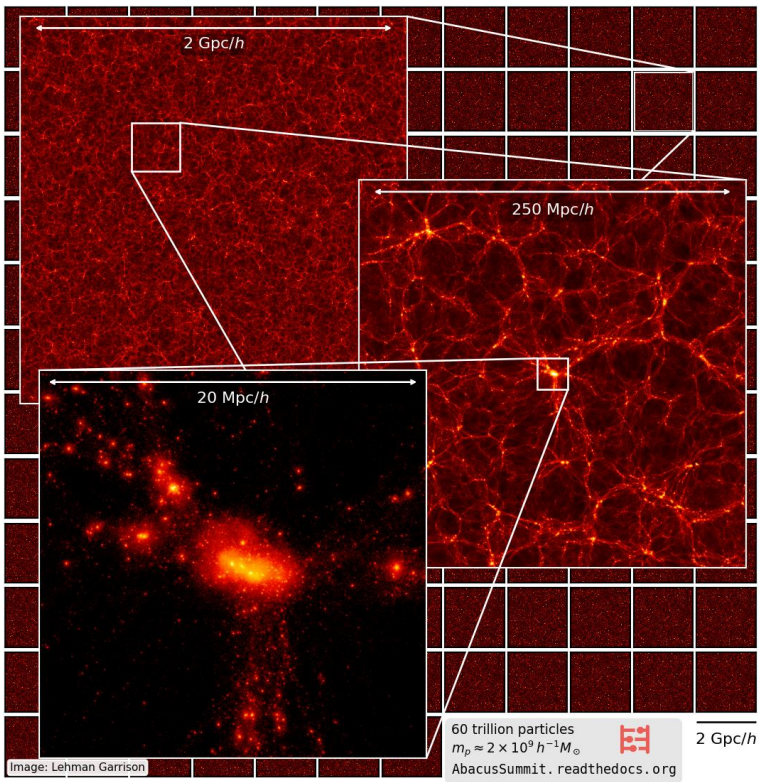

Figure 2. Abacus-Summit N-body simulation: large-scale structure from 2 Gpc/h box to resolved halo (20 Mpc/h)

1.5. Preview of the work

We present an analytic HMF emulator with improved flexibility and stability, calibrated against Abacus-Summit simulations to achieve percent-level precision across wide mass, redshift, and

cosmological parameter ranges. Section 2 reviews HMF theory, Section 3 details our simulation analysis, Section 4 develops the emulator framework, and Section 5 presents results and limitations, with conclusions in Section 6.

2. Theory of Structure Formation

In this section, we first present the statistical formalism describing density perturbations in the matter distribution of the Universe, followed by an overview of dark matter halo formation and the basic theory underlying the HMF.

2.1. Perturbations of cosmic density fields

A fundamental principle of cosmology is that, on the largest scales, the matter in the Universe is distributed in a homogeneous and isotropic manner. However, quantum fluctuations in the early Universe acted as seeds for small-scale tiny density perturbations on this smooth background, which subsequently grew under the influence of gravity to form the large-scale structure we observe today. These perturbations can be statistically characterized within the framework of cosmological perturbation theory, providing a quantitative description of their amplitude, scale dependence, and evolution over cosmic time.

At a given epoch of the Universe, characterized by the scale factor $a = \frac{1}{1+z}$ at cosmological redshift z, its average matter content is described by the mean matter density $\bar{\rho}_{\mathrm{m}}(a)$. The spatial distribution of matter is represented by the matter density field $\rho_{\mathrm{m}}(\vec{x}, a)$, defined at each comoving coordinate $\vec{x}$. To quantify deviations from homogeneity, we introduce the dimensionless matter density contrast $\delta_{\mathrm{m}}(\vec{x}, a)$, written as

$$\delta_{\mathrm{m}}(\vec{x}, a) = \frac{\rho_{\mathrm{m}}(\vec{x},a)}{\bar{\rho}_{\mathrm{m}}(a)} - 1, \tag{1}$$

Which measures the local fractional overdensity or underdensity relative to the cosmic mean. When the matter density contrast is much less than unity, $|\delta_{\mathrm{m}}(\vec{x}, a)| \ll 1$, the growth of cosmic structures can be accurately described using linear perturbation theory.

A standard statistical tool for characterizing the large-scale matter distribution is the matter power spectrum. In the linear regime, the matter power spectrum $P_{\mathrm{mm}}^{\mathrm{L}}(k, a)$ at wavenumber k and scale factor a is given by

$$P_{\mathrm{mm}}^{\mathrm{L}}(k, a) = \left|\tilde{\delta}_{\mathrm{m}}(\vec{k}, a)\right|^2, \tag{2}$$

Where $\tilde{\delta}_{\mathrm{m}}(\vec{k}, a)$ s the Fourier transform of the matter density contrast in real space $\delta_{\mathrm{m}}(\vec{x}, a)$.

To quantify the amplitude of density fluctuations on a given scale, we define the mass variance $\sigma_{\mathrm{m}}^2(M, a)$ for halos of mass M at scale factor a. This quantity plays a central role in structure formation theory and in predicting halo abundances through the HMF. The mass variance is computed by filtering the linear matter power spectrum with a real-space spherical top-hat window,

$$\sigma_{\mathrm{m}}^2(M, a) = \int_0^\infty P_{\mathrm{mm}}^{\mathrm{L}}(k, a) \left|\widetilde{W}(kR_{\mathrm{m}})\right|^2 \frac{k^2\,\mathrm{d}k}{2\pi^2}, \tag{3}$$

Where $\widetilde{W}(kR_{\mathrm{m}})$ is the Fourier transform of the top-hat filter of radius R_{m},

$$\widetilde{W}(kR) = \frac{3}{(kR_{\mathrm{m}})^3}[\sin(kR_{\mathrm{m}}) - (kR_{\mathrm{m}})\cos(kR_{\mathrm{m}})]. \tag{4}$$

In real space, the top-hat filter is defined as

$$W(x|R) = \begin{cases} \frac{3}{4\pi R^3} & x \leq R_{\mathrm{m}} \\ 0 & X > R_{\mathrm{m}} \end{cases}, \tag{5}$$

Which smooths the overdensity field $\delta_{\mathrm{m}}(\vec{x}, a$ over the scale R_{m}, isolating fluctuations on that characteristic size.

For a halo of mass M, the smoothing scale R_{m} is chosen as the Lagrangian radius, defined by

$$R_{\mathrm{m}}(M) = \frac{3M}{4\pi\bar{\rho}_{\mathrm{m}}}. \tag{6}$$

2.2. Beyond linear structure formation

When $|\delta_{\mathrm{m}}(\vec{x}, a)| \gg 1$, the system enters the non-linear regime of structure formation. In this regime, the strong gravitational field associated with high local overdensity drives gravitational collapse, leading to the formation of self-gravitating bound structures known as dark matter halos. In the simplified spherical collapse model, which assumes spherical symmetry during halo formation, the onset of collapse is characterized by a critical overdensity δ_{c} – defined within linear perturbation theory – that marks the threshold for collapse. This allows the mass variance from linear theory to be related to the properties of virialised halos. A commonly adopted value is

$$\delta_{\mathrm{c}} = 1.686. \tag{7}$$

An important quantity in analytic halo formation models is the peak height μ, which measures the significance of a density fluctuation of mass scale M at cosmic epoch a. It is defined as the ratio of δ_{c} to the RMS amplitude of fluctuations, $\sigma_{\mathrm{m}}(M, a)$. Larger values of μ_{m} correspond to rarer, more extreme peaks in the initial density field that are capable of collapsing into halos of mass M at epoch a:

$$\mu_{\mathrm{m}}(M, a) = \frac{\delta_{\mathrm{c}}}{\sigma_{\mathrm{m}}(M,a)}. \tag{8}$$

2.3. Formalism of halo abundance

To predict the abundance of halos at a given mass scale using the statistical properties of the matter density field, cosmologists employ the halo mass function (HMF), typically written as, $\frac{\mathrm{d}n}{\mathrm{dlog}_{10}M}$, which quantifies the comoving number density of dark matter halos per logarithmic mass interval. A common reformulation introduces a dimensionless mass function, $f_{\mathrm{m}}(M, a)$, allowing the HMF to be expressed as

$$\frac{\mathrm{d}n}{\mathrm{dlog}_{10}M} = f_{\mathrm{m}}(M, a)\ \frac{\bar{\rho}_{\mathrm{m}}}{M}\ \frac{\mathrm{dln}\mu_{\mathrm{m}}}{\mathrm{dlog}_{10}M}, \tag{9}$$

Where $\bar{\rho}_{\mathrm{m}}$ denotes the present-day mean matter density of the Universe, and the Jacobian factor $\frac{\mathrm{dln}\mu_{\mathrm{m}}}{\mathrm{dlog}_{10}M}$ accounts for the transformation between variables. This formulation provides a crucial link between cosmological theory and observations of the large-scale structure.

A widely used simplification in HMF modeling is the universality assumption, which asserts that the dimensionless mass function $f_{\mathrm{m}}(M,a)$ depends only on the peak height $\mu_{\mathrm{m}}(M,a)$. Therefore,it can be written as $f[\mu(M,a)]$. Early analytic models provide physically motivated fitting forms. In particular, using spherical or ellipsoidal collapse considerations, one can express

$$\frac{f_{\mathrm{m}}(\mu)}{\mathcal{F}} = \mu_{\mathrm{m}}^{\mathcal{A}}(1+\mathcal{B}\,\mu_{\mathrm{m}}^{\mathcal{C}})\exp\left(-\frac{1}{2}\mu_{\mathrm{m}}^{2}\right), \tag{10}$$

Where $\mathcal{A}$, $\mathcal{B}$, $\mathcal{C}$ and $\mathcal{F}$, are model parameters. At a fixed epoch, the HMF exhibits a steep exponential tail at high masses and an approximate power-law behavior at low masses. As redshift increases, high-mass halos become exponentially rarer while low-mass ones remain more abundant, reflecting hierarchical structure growth.

Under the universality assumption, both $f_{\mathrm{m}}(\mu_{\mathrm{m}})$ and its parameters are treated as constant – once calibrated, they can be applied across cosmologies and epochs. However, this assumption is only approximate. Deviations of order $10\% - 50\%$, depending on redshift, mass range, or cosmology, have been reported.

In numerical simulations, dark matter halos can be identified using several methods. A widely used approach is the Friends-of-Friends (FoF) algorithm, which links particles into groups based on interparticle separations: any two particles separated by less than a specified fraction, named the linking length b_{FoF}, of the mean interparticle distance are assigned to the same group. For this choice of b_{FoF}, FoF groups typically enclose an average overdensity of $\sim 80\bar{\rho}_{\mathrm{m}}$, though the exact value depends on the halo concentration and particle distribution.

A distinct and empirically grounded definition is the Spherical Overdensity (SO) method, which identifies halos by enlarging spheres around density peaks until the mean density within them meets a predetermined overdensity threshold Δ in comparison relative to a reference density. A typical selection for the reference density is the critical density $\rho_{\mathrm{c}} = \frac{3H^2(a)}{8\pi G}$ of the Universe, where a is the scale factor and $H(a)$ denotes the Hubble parameter at that particular epoch. The mass of the halo M_{Δ} is then described, with R_{Δ} representing the radius of SO halos that meet the specified overdensity Δ. Each methodology has its advantages and drawbacks: FoF can identify complex, filamentary structures but might include bridged or non-spherical clusters, whereas SO offers clearly delineated spherical boundaries that align better with observations, although it may overlook particles in extended substructures. These definitions can produce systematically different halo masses and boundaries, particularly in dense or merging scenarios.

To enhance the flexibility of the halo mass function (HMF), several modifications have been proposed. One study incorporated redshift evolution into the fitting function, calibrated using spherical overdensity (SO) halo definitions across various density thresholds Δ, achieving $\sim 10\%$ accuracy for masses between 10^{11}–$10^{15}M_{\odot}$ in a ΛCDM cosmology. However, the amplitude of the universal function was found to decrease by 20%–50% from $z = 0$ to $z \approx 2.5$. Another study extended the HMF calibration using simulations under ΛCDM and wCDM cosmologies, improving the high-mass tail. Further work expanded the calibration up to $z \sim 30$, providing separate fits for friends-of-friends (FoF) and SO halo finders while maintaining $\sim 20\%$ accuracy across redshifts and halo definitions. In all cases, the modified fitting form can be written in a unified manner:

$$\frac{f_{\mathrm{m}}(\mu_{\mathrm{m}})}{\mathcal{F}} = \mu_{\mathrm{m}}^{\mathcal{A}}(1+\mathcal{B}\,\mu_{\mathrm{m}}^{\mathcal{C}})\exp(-\mathcal{D}\,\mu_{\mathrm{m}}^{2}), \tag{11}$$

Where the parameters $\mathcal{A}$, $\mathcal{B}$, $\mathcal{C}$, $\mathcal{D}$ and $\mathcal{F}$ now vary with both redshift and the overdensity threshold Δ. This framework aligns theoretical predictions more closely with observational mass definitions

and maintains accuracy within a few $\times 10\%$ over extended mass and redshift ranges-rendering it particularly valuable for studies of the early Universe and proto-cluster formation.

However, additional factors contributing to non-universality – such as the definition of halo mass, total neutrino masses, scale gradient of initial power spectra, and dynamical dark energy equation of state – must still be meticulously considered when extending HMF models beyond the standard $\Lambda\mathrm{CDM}$ framework. As elaborated in the following sections, we will provide further enhancements to the analytical expression of the HMF to refine precision across an even broader spectrum of halo masses, redshifts, and cosmologies.

3. Simulation Data Processing

We initially outline the key properties of the Abacus-Summit simulations in this section, followed by a description of the methodology for measuring halo masses under multiple definitions and for computing the associated summary statistics.

3.1. Abacus-Summit simulations

This work utilizes the Abacus-Summit simulation suite, one of the largest cosmological simulations designed to meet DESI requirements. The base runs employ 6912^3 particles (330 billion) in a $2\,\mathrm{Gpc}/h$ box with $2 \times 10^9\, M_\odot/h$ mass resolution, totaling over 140 runs with 60 trillion particles including light-cones and resolution variants. The suite spans 97 cosmological models beyond $\Lambda\mathrm{CDM}$, incorporating variations in dark energy ($w_0,\ w_a$), relativistic species (N_{eff}), power spectrum running (α_s), and parameters like $\omega_{\mathrm{CDM}},\ \omega_{\mathrm{b}},\ \sigma_8,\ n_s$, and H_0, enabling interpolation across an 8D parameter space for emulator development.

Group finding in Abacus-Summit is performed at eleven primary redshift snapshots – namely $z = 0.10,\ 0.20,\ 0.30,\ 0.40,\ 0.50,\ 0.80,\ 1.10,\ 1.40,\ 1.70,\ 2.00$, and 2.50 – with an additional set of approximately twenty-two secondary snapshots providing finer temporal sampling. At each primary snapshot, comprehensive halo catalogs, subsample of particles, and associated data products are generated to support detailed analyses of halo properties and cosmological evolution. The suite offers a rich set of outputs: halo catalogs include Friends-of-Friends (FoF) Level 0 (L0) groups and spherical-overdensity Level 1 (L1) halos, complete with positions, velocities, and merger histories; subsample of particles enable accurate reconstruction of density fields; and light-cone outputs are tailored for synthetic survey applications. In our analysis of the halo mass function (HMF), we make extensive use of the L1 halo catalogs.

Halo identification is conducted in real-time using the CompaSO algorithm – a competitive assignment to spherical overdensity method refined for effective operation in dense environments. The process begins by calculating kernel density estimates around particles, utilizing a smoothing radius of 0.4 times the interparticle spacing. Subsequently, L0 FoF groups are identified among particles with an overdensity $\Delta > 60$. Within each L0 group, the highest-density particle is chosen as the nucleus, and a SO region is expanded until the enclosed density drops below the reference overdensity, counting only L0 particles. Particles within this radius constitute an L1 halo; additional nuclei are seeded among remaining eligible high-density particles. Any overlapping assignments are resolved through density comparisons, without explicit gravitational unbinding.

Optionally, within each L1 halo, a secondary overdensity search identifies Level 2 (L2) substructures with a density threshold of 800 times the mean density. The center of mass of the largest L2 structure is used to define the L1 halo center, although only L1 halos are cataloged. Merger trees are subsequently constructed during post-processing by tracking particle IDs across snapshots. This permits the historical linkage of halos and facilitates additional cleaning procedures that address issues of excessive deblending or erroneous halo identifications.

3.2. Conversion of halo masses

The CompaSO algorithm offers substantial advantages in dense matter fields and is significantly more computationally efficient than traditional halo finders that require calculating gravitational potentials for unbinding particles. As an on-the-fly method, CompaSO avoids the computationally intensive unbinding step and reduces memory and storage overhead. Furthermore, by using competitive assignment of particles within SO, it effectively mitigates the issue of overlapping halos characteristic of conventional SO approaches. A potential drawback, however, lies in the fact that the resulting halos do not all conform to a single fixed overdensity threshold. Due to particle competition and reassignment in the algorithm, the effective overdensity at halo edges may vary between objects, complicating direct comparisons and consistent modeling of the resulting HMF.

Therefore, we use halos identified by the CompaSO algorithm but convert their masses to a common SO definition, enabling more direct comparisons between theoretical predictions and future observations. To achieve this, we assume that the inner matter distribution of dark matter halos follows the Navarro-Frenk-White (NFW) profile, which provides an almost universal description of the spherically averaged halo density profile:

$$\rho(r) = \frac{\rho_s}{\left(\frac{r}{r_s}\right)\left(1+\frac{r}{r_s}\right)^2}, \tag{12}$$

Where ρ_s is the characteristic density, and r_s is the scale radius that determines the shape of the profile. Given ρ_s and ρ_s, the NFW profile can be integrated to obtain the enclosed mass within radius r:

$$M(<r) = 4\pi\rho_s r_s^3 \left[\ln\left(1+\frac{r}{r_s}\right) - \frac{\frac{r}{r_s}}{1+\frac{r}{r_s}}\right]. \tag{13}$$

Under an SO definition with overdensity threshold Δ, the halo mass M_Δ and radius R_Δ satisfy

$$M_\Delta = \frac{4\pi\Delta}{3}\rho_c R_\Delta^3, \tag{14}$$

Where ρ_c is the critical density of the Universe under scale factor a. Matching this to the NFW mass profile gives

$$M_\Delta = 4\pi\rho_s r_s^3 \left[\ln\left(1+\frac{R_\Delta}{r_s}\right) - \frac{\frac{R_\Delta}{r_s}}{1+\frac{R_\Delta}{r_s}}\right]. \tag{15}$$

For convenience, we define the halo concentration parameter at overdensity Δ as

$$c_\Delta = \frac{R_\Delta}{r_s} \tag{16}$$

Which quantifies how centrally concentrated the halo mass is. Using this notation, the NFW mass profile can be expressed in a normalized form as

$$M(<u) = M_\Delta \frac{m(c_\Delta u)}{m(c_\Delta)}, \tag{17}$$

Where the dimensionless radius is $u \equiv \frac{r}{R_\Delta}$, and the dimensionless enclosed mass profile is

$$m(x) = \ln(1+x) - \frac{x}{1+x}. \tag{18}$$

Based on the cleaned Abacus-Summit catalogs of all L1 halos across all redshift snapshots, we have the measured halo mass M_Δ and R_Δ, but the overdensity threshold Δ varies from halo to halo. This formulation enables us to convert all halos to a common SO overdensity threshold Δ_*, yielding uniformly defined masses M_{Δ_*} and radius R_{Δ_*}, and ensuring consistent halo mass definitions across the catalogs.

We estimate the concentration c_Δ of each halo assuming an NFW profile, using the radius of maximum circular velocity, $R_{\rm max}$, as a proxy. For an NFW halo, $R_{\rm max}$ is related to c_Δ via

$$u_{\rm max} \equiv \frac{R_{\rm max}}{R_\Delta} \approx \frac{2.1626}{c_\Delta}. \tag{19}$$

From this process, we determine c_Δ for each halo and subsequently determine $u_{\Delta_*} \equiv \frac{R_{\Delta_*}}{R_\Delta}$. This is achieved by aligning the NFW mass profile described in Equation 3.6 with the SO definition at Δ_*, and we have

$$M_{\Delta_*} = M_\Delta \frac{m(c_\Delta u_{\Delta_*})}{m(c_\Delta)} = \frac{4\pi\Delta_*}{3} \rho_{\rm c} \left(u_{\Delta_*} R_\Delta\right)^3, \tag{20}$$

Where the right-hand equals uses the definitions of SO at overdensity threshold Δ_*. After combining with Equation 3.3, the above equation simplifies to the dimensionless form

$$\frac{m(c_\Delta u_{\Delta_*})}{m(c_\Delta)\, u_{\Delta_*}^3} = \frac{\Delta_*}{\Delta}. \tag{21}$$

For each halo, after solving Eq. 3.10 numerically for u_{Δ_*}, we then compute

$$R_{\Delta_*} = u_{\Delta_*} R_\Delta, \quad M_{\Delta_*} = M_\Delta \frac{m(c_\Delta u_{\Delta_*})}{m(c_\Delta)}, \quad c_{\Delta_*} = c_\Delta u_{\Delta_*}. \tag{22}$$

This procedure yields halo properties under a uniform overdensity threshold Δ_*, enabling consistent comparisons across the catalog.

In this work, we adopt six different SO thresholds, Δ_*, for defining halo masses. These include the 100c, $\Delta_* = 100$; 200c, $\Delta_* = 200$; 200m, $\Delta_* = 200 \cdot \Omega_{\rm m}(a)$; 500c, $\Delta_* = 500$; 1000c, $\Delta_* = 1000$ and virial definition, $\Delta_* = \Delta_{\rm v}(a)$. Halo masses are converted to each of these definitions using the procedure described in the previous section. As an example, Fig. 3 presents the halo mass–concentration relation for the virial definition across multiple redshift snapshots. In each panel, our results from the Abacus-Summit simulations (black lines) are compared to established fitting functions from the literature (colored lines).

These comparisons reveal the redshift evolution of the mass–concentration relation, showing strong agreement with existing models for halos in the mass range $\sim 3 \times 10^{12} - 10^{15}\, M_\odot$, confirming the robustness of our mass conversion approach. However, at lower masses ($\lesssim 3 \times 10^{12}\, M_\odot$), concentrations are systematically underestimated, likely due to resolution effects from limited particle

counts affecting halo radial profile measurements. This bias in concentration estimation at low masses will be addressed in the subsequent discussion of its impact on HMF measurements.

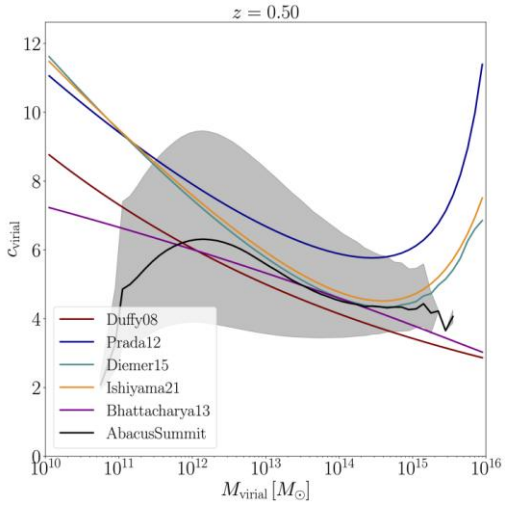

Figure 3. Example of the mass-concentration relationship

3.3. Estimation of binned quantities

After obtaining the mass of individual halos under multiple SO definitions, we use the following estimator to measure the discrete HMF $\hat{n}(M, a)$ from the Abacus-Summit simulations, expressed as

$$\hat{n}(M, a) = \frac{\Delta N(M,a)}{L^3\, \Delta \log_{10} M}, \tag{23}$$

Where $\hat{n}$ denotes the simulation-derived estimator, L refers to the comoving boxsize of the simulation for analysis, and we count the number of halos ΔN within each logarithmic internal $\Delta \log_{10} M$. We adopt $\mathcal{N}_{\rm m} = 60$ bins of halo mass within the range $10^{10}\, M_\odot \equiv M_1 \leq M \leq M_2 \equiv 10^{16}\, M_\odot$ with logarithmic spacing, corresponding to $\Delta \log_{10} M = \frac{\log_{10}(M_2/M_1)}{\mathcal{N}_{\rm m}} = 0.1$. In Fig. 4, we display the HMF at different redshift snapshots under the fiducial cosmology with base comoving volume and particle mass resolutions. The panels illustrate how the choice of overdensity threshold Δ_* affects both the normalization and shape of the HMF at fixed redshift. With increasing Δ_*, the definition of halo masses are more centered around the density peaks, thus producing lower halos masses and fewer number of halos at given mass range. This comparison providing a basis for consistent comparisons with theoretical models and observationally inferred halo abundances.

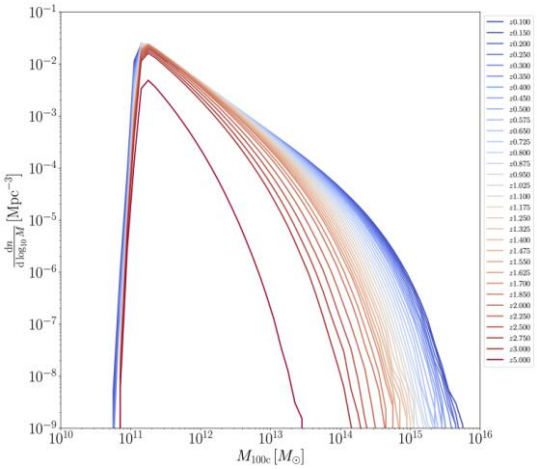

Figure 4. HMFs $\frac{{\rm d}n}{{\rm d}\log_{10} M}$ from the Abacus-Summit simulations for all available redshift snapshots

Moreover, the Abacus-Summit suite comprises 25 versions of the fiducial cosmology, all maintaining identical comoving volumes and particle mass resolutions but differing in their initial conditions. This allows for an examination of the effects of cosmic variance. Utilizing this ensemble, we calculate the covariance matrix $\hat{\Sigma}(M, a|M', a')$ for two separate HMFs at varying halo masses and redshifts (M, a) and (M', a'), represented as

$$\hat{\Sigma}_n(M, a|M', a') = \langle [n(M, a) - \langle n \rangle (M, a)] \cdot [n(M', a') - \langle n \rangle (M', a')] \rangle, \tag{24}$$

Where $\langle \cdot \rangle$ denotes the ensemble average over the 25 realizations. In Fig. 5, we compare the fractional uncertainties from these simulation-based estimates with those from the theoretical expectation under Poisson statistics, given by

$$\hat{\sigma}_n(M, a) = \frac{\sqrt{\Delta N(M,a)}}{L^3 \, \Delta \log_{10} M}. \tag{25}$$

The strong correlation between the simulation outcomes (solid lines) and the Poisson predictions (dashed lines) suggests that Poisson noise effectively characterizes the statistical uncertainties in the HMF across various redshift snapshots and SO halo mass definitions. Moreover, owing to the restricted number of simulations at our disposal, the simulation-derived estimations exhibit significant numerical instabilities. Additionally, we do not have access to further simulations across varying initial conditions for different cosmological models. Therefore, for the sake of simplicity, we adopt Poisson errors when estimating the HMF uncertainties for all cosmological models as a foundation for subsequent likelihood analyses.

In addition, we find, at the high-mass end, uncertainties can reach $\gtrsim 10\%$, reflecting the dominance of sample variance and the small-number statistics of rare halos. In contrast, at the low-mass end, statistical uncertainties are suppressed to the sub-percent level ($\lesssim 1\%$), and systematic effects associated with resolution limits and halo finding become the dominant contributors to the error budget, as discussed below.

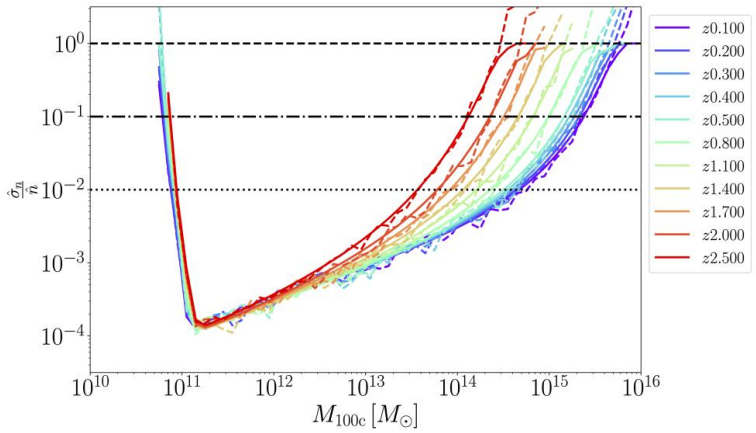

Figure 5. The fractional uncertainties of HMFs $\frac{\hat{\sigma}_n}{\hat{n}}$ from the Abacus-Summit simulations

The Poisson model implicitly assumes that variances are independent across different halo mass bins and redshift snapshots. To assess this assumption, we compute the correlation matrices $\hat{\Xi}(M, a|M', a')$, defined as

$$\hat{\Xi}(M, a|M', a') = \frac{\hat{\Sigma}(M,a|M',a')}{\sqrt{\hat{\Sigma}(M,a|M,a)\,\hat{\Sigma}(M',a'|M',a')}}. \tag{26}$$

Where $\hat{\Sigma}$ is the covariance matrix defined previously. As shown in Fig. 6, we present the correlation matrices of the HMFs across all primary redshift snapshots for the virial mass definition. The color scale indicates the strength of correlations between halo abundances, with each small panel corresponding to either the auto-correlation at a single redshift (diagonal panels) or the cross-correlation between two different redshifts (off-diagonal panels). Within each panel, the diagonal entries represent the variance of halo counts in individual mass bins, while the off-diagonal entries quantify the degree of correlation between fluctuations in different mass bins.

The auto-correlation panels (diagonal blocks), which largely determine the overall structure of the correlation matrices, show that correlations between different halo mass bins are negligible, particularly for massive halos. This behavior arises because halo abundances in distinct mass ranges are primarily governed by independent Poisson statistical processes, as already illustrated for high-mass halos in Fig. 5. A mild degree of correlation is observed among low-mass halos, but as discussed previously, the error budget in this regime is dominated by systematic rather than statistical uncertainties, rendering these correlations non-critical for our analysis.

In the off-diagonal panels, we find non-negligible correlations between HMFs at different redshifts, especially for low-redshift pairs. This behavior is consistent with the hierarchical model of structure formation: in the late-time Universe, non-linear processes such as mergers, accretion, and interactions lead to correlated halo abundances across epochs. However, given the limited number of covariance realizations available, we do not attempt to model these cross-redshift correlations explicitly in our subsequent likelihood analysis. Instead, we continue to adopt the assumption of independent Poisson statistics, deferring the inclusion of full correlation matrices to future work.

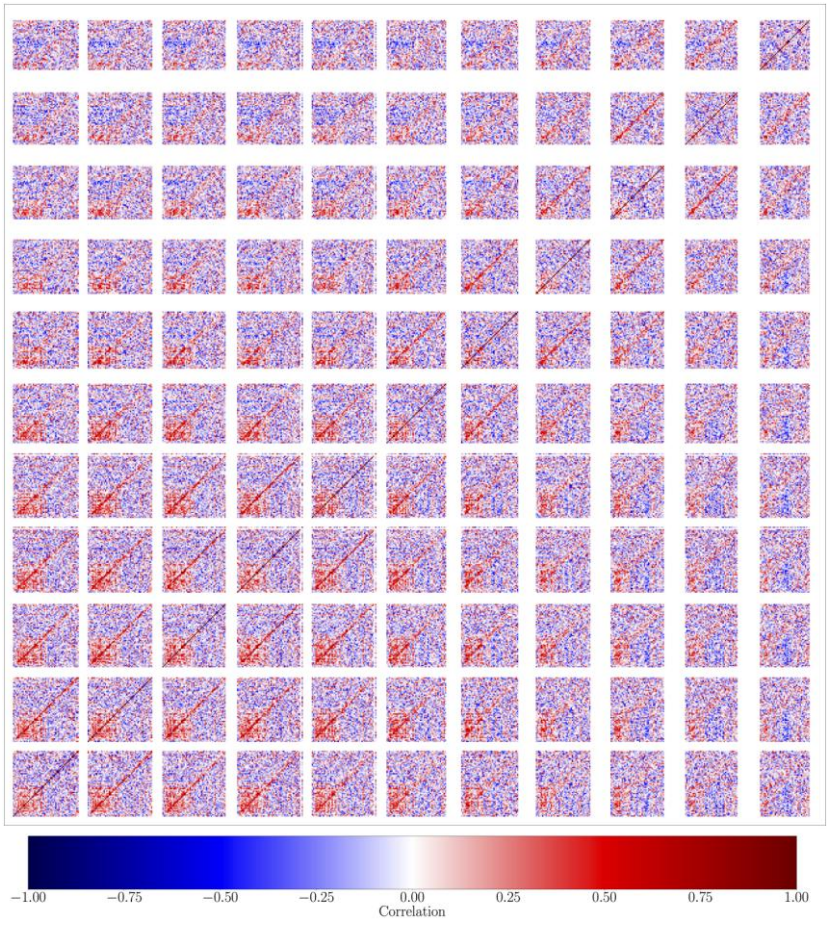

Figure 6. Cross-redshift correlation matrices of the halo mass function (virial definition) from Abacus-Summit simulations

At the low-mass end, $M \lesssim 10^{11}\, M_{\odot}$, the measured HMF exhibits a sharp decline due to the limited mass resolution of the simulations, which is insufficient to robustly resolve halos of such small masses.

At the high-mass end, the number of halos per mass bin becomes small, making the measurements susceptible to sample variance. In both regimes, the resulting low Signal-to-Noise (SNR) estimates can bias subsequent modeling. To mitigate these effects, we apply an initial filtering step: at the low-mass end we impose a minimum halo mass corresponding to 100 particles in a given simulation, $M_{\mathrm{l}} = 100 \times M_{\mathrm{p}}$, where M_{p} is the particle mass. At the high-mass end, we require that each mass bin contains at least 100 halos, $\Delta N(M_{\mathrm{u}}) = 100$. This filtering procedure ensures that our analysis excludes poorly measured bins at both extremes of the mass range, thereby reducing systematic effects in the subsequent modeling of the HMF.

3.4. Correction of systemic effects

One major systematic effect that must be corrected is the finite mass resolution of the simulations. Since the particles have non-negligible mass, the formation and evolution of small halos are not fully resolved, leading to biases in the HMF. To quantify and mitigate this effect, we make use of subsets of the Abacus-Summit simulations that share the same cosmological parameters but differ in particle mass resolution. The aim of this correction is not to completely remove resolution effects – which is impossible given that particle mass cannot be infinitesimal – but rather to homogenize all simulations to a common effective resolution. Specifically, we choose to calibrate all runs to the highest available resolution, thereby minimizing resolution-induced biases in the HMF.

Abacus-Summit provides three levels of particle mass resolution: the base setup with particle mass $2 \times 10^9\, h^{-1}\, M_{\odot}$, a high resolution case with six times lower particle mass, and a low resolution case with 27 times higher particle mass than the base configuration. We first compare simulations with identical cosmology but different initial conditions, run at base and high resolutions, respectively. From these, we compute the ratio of the binned HMFs, defined as

$$\hat{\mathcal{R}}^{\mathtt{lower}}(M, a) = \frac{\hat{n}^{\mathtt{base}}(M,a)}{\hat{n}^{\mathtt{high}}(M,a)}, \tag{27}$$

Which serves as a correction factor to map HMFs measured at base resolution onto their high resolution equivalents.

Similarly, by comparing simulations with low and base resolutions, we compute

$$\hat{\mathcal{R}}^{\mathtt{upper}}(M, a) = \frac{\hat{n}^{\mathtt{low}}(M,a)}{\hat{n}^{\mathtt{base}}(M,a)}, \tag{28}$$

Which enables us to adjust HMFs from low resolution simulations to the base resolution, and subsequently to the high resolution, by incorporating $\hat{\mathcal{R}}^{\mathtt{lower}}(M, a)$. In both scenarios, the ratios are calculated across multiple realizations with varied initial conditions, ensuring robustness against cosmic variance.

This calculation is performed only at the primary redshift snapshots, since their redshift values are precisely defined. In contrast, the secondary snapshots do not correspond to unique redshifts due to the limited temporal resolution of the simulations. To reduce noise in the measured ratios, as well as to allow for mild interpolation and extrapolation across halo masses and redshifts, we develop an empirical analytic model to describe their evolution. Specifically, we parameterised the dependence on halo mass through the logarithmic variable

$$x = \log_{10}\left(\frac{M}{M_1}\right),\ 0 \le x \le 6, \tag{29}$$

And model the resolution correction ratio $\mathcal{R}(M, a)$ as

$$\mathcal{R} = 1 + \frac{p\,(x-r)+q\,(x-r)}{1+\exp[+s\,(x-r)]} + \frac{t\,(x-r)}{1+\exp[-s\,(x-r)]}, \tag{30}$$

Where the coefficients p, q, r, s, t capture the redshift dependence of the correction. Their evolution with redshift is expressed as quadratic functions of the logarithm of the scale factor, $\ln a = \ln\left(\frac{1}{1+z}\right)$:

$$\begin{aligned} p &= p_0 + p_1 \ln a + p_2 (\ln a)^2, \\ q &= q_0 + q_1 \ln a + q_2 (\ln a)^2, \\ r &= r_0 + r_1 \ln a + r_2 (\ln a)^2, \\ s &= s_0 + s_1 \ln a + s_2 (\ln a)^2, \\ t &= t_0 + t_1 \ln a + t_2 (\ln a)^2. \end{aligned} \tag{31}$$

Utilizing a parameterised model characterized by $\mathcal{N}_{\boldsymbol{\phi}} = 15$ free parameters $\boldsymbol{\phi}$, where bold symbols denote vectors, we employ Markov Chain Monte Carlo (MCMC) to optimize the coefficients. MCMC is an efficient Bayesian algorithm adept at exploring high-dimensional parameter spaces to determine the value set that statistically minimizes the loss function robustly.

Here, we use assume flat priors with Uniform distributions,

$$\mathcal{P}(\boldsymbol{\phi}) \sim \mathcal{U}(-5, +5), \tag{32}$$

For all modeling parameters, and assume the Gaussian form of likelihood function,

$$\mathcal{L} = \ln\mathcal{P}\left(\hat{\mathcal{R}} \mid \boldsymbol{\phi}\right) = -\frac{1}{2}\ln[(2\pi)^{\mathcal{N}_{\mathcal{R}}}\,|\boldsymbol{\Sigma}_{\mathcal{R}}|] - \frac{1}{2}\left[\hat{\mathcal{R}} - \mathcal{R}(\boldsymbol{\phi})\right]^{\dagger} {\boldsymbol{\Sigma}_{\mathcal{R}}}^{-1} \left[\hat{\mathcal{R}} - \mathcal{R}(\boldsymbol{\phi})\right], \tag{33}$$

Where $\hat{\mathcal{R}}$ are the measured ratios, $\mathcal{R}(\boldsymbol{\phi})$ are the model predictions under parameter $\boldsymbol{\phi}$, $\mathcal{N}_{\mathcal{R}}$ is the dimensionality of the data, and $\boldsymbol{\Sigma}_{\mathcal{R}}$ denotes the covariance matrix. In the first-order approximation, we include only the diagonal terms based on Poisson uncertainties, neglecting cross-covariances as discussed previously. The optimization is performed with the affine-invariant MCMC ensemble sampler emcee, using 1024 walkers and 1024 steps. We discard the first 50% of the chains as burn-in and adopt the maximum-posterior point $\boldsymbol{\phi}_* = \mathrm{argmax}\left[\mathcal{P}\left(\boldsymbol{\phi} \mid \hat{\mathcal{R}}\right)\right]$ as the best-fitting parameter set, which are listed in Tabs. 1 and 2 for lower and upper cases, respectively, under multiple halo mass definitions.

As summarized above, the best-fitting parameters of our resolution-correction model $\mathcal{R}(M, a)$, vary across the different SO definitions, reflecting the fact that halo masses defined with distinct overdensity thresholds respond differently to the effects of finite particle resolution. This dependence highlights the necessity of calibrating separate correction functions for each SO definition in order to achieve consistent results.

Table 1. Best-fitting parameters obtained from the MCMC optimization of the lower resolution-correction model, $\mathcal{R}^{\mathrm{lower}}(M,a)$, for six SO definitions: 100c, 200c, 200m, 500c, 1000c, and Virial. Each parameter set describes the redshift-dependent correction ratio applied to homogenize HMFs across different simulation resolutions

ϕ	100c	200c	200m	500c	1000c	virial
p_0	-0.0422	-0.0954	-0.1449	0.4926	0.6352	-0.1049
p_1	0.2522	0.1360	0.0301	-0.4150	-0.8697	0.1848
p_2	0.0532	-0.0442	-0.1788	-0.3013	-0.6290	0.0207
q_0	0.1288	0.0806	0.3444	-0.4370	-0.7219	0.1421
q_1	-0.7023	-0.2895	0.2267	-0.2525	0.2080	-0.3486
q_2	-0.2352	0.0536	0.2073	0.2851	0.5138	-0.0268
r_0	0.4409	1.2575	0.7561	0.9478	0.8698	0.7718
r_1	-1.1527	0.2942	-0.5086	-0.6231	-0.5040	-0.6776
r_2	-0.4969	0.0901	-0.2249	-0.5193	-0.6928	-0.3843
s_0	0.2363	0.3678	0.8195	1.8535	1.7674	0.3373
s_1	-2.4408	-0.8803	0.4833	-1.2549	-1.2580	-1.2388
s_2	-1.6155	-0.5433	0.1957	-0.8720	-1.0282	-0.8138
t_0	-0.0029	0.0497	0.0038	-0.0116	-0.0160	0.0481
t_1	0.0014	0.0712	-0.0262	0.0104	0.0133	0.0833
t_2	-0.0013	0.0540	0.1045	-0.0039	-0.0047	0.0543

Table 2. Best-fit parameters from MCMC optimization of the lower resolution-correction model $\mathcal{R}^{\mathrm{upper}}(M,a)$ for six SO definitions: 100c, 200c, 200m, 500c, 1000c, and Virial, describing redshift-dependent HMF corrections across resolutions.

ϕ	100c	200c	200m	500c	1000c	virial
p_0	-0.1946	0.4796	-0.3648	0.0304	-0.2761	0.4283
p_1	0.6187	-0.3226	0.0279	-0.6317	0.3788	-0.4752
p_2	2.0277	0.3309	-0.0748	-0.2705	0.4167	0.0202
q_0	0.3102	-0.0510	0.5517	-0.3285	-0.3401	0.0799
q_1	-1.5645	-0.1249	0.3257	0.5711	0.2378	0.0133
q_2	-1.4921	0.1003	0.5452	-0.2799	0.3031	0.4515
r_0	2.2138	2.0136	2.2109	4.0696	3.8453	1.7735
r_1	0.4220	0.4631	0.0804	0.5025	0.5677	-0.2445
r_2	0.1703	0.2060	-0.0818	0.3774	0.3701	-0.0765
s_0	0.3675	1.2495	0.6001	-1.0342	0.1475	1.2645
s_1	-1.3125	-0.2532	0.3217	-0.5528	-0.7900	-0.4404
s_2	-0.1362	-0.1832	0.0136	-0.0978	-0.0695	-0.3107
t_0	0.0623	-0.0615	0.0686	0.1189	0.1971	-0.0433
t_1	0.4059	0.0059	-0.1672	-0.4585	-0.0978	0.0144
t_2	0.2853	-0.0397	-0.0915	0.0554	-0.5475	-0.0349

Based on these best-fitting parameters, we compute the optimized resolution-correction model, $\mathcal{R}^{\mathrm{lower}}(M,a)$ and $\mathcal{R}^{\mathrm{upper}}(M,a)$, shown in Figs. 7 and 8, together with direct estimates from

simulations. The excellent agreement between the analytic model and simulation measurements demonstrates the effectiveness of our formalism in mitigating resolution effects over the halo mass range where the HMF is robustly estimated. Moreover, the smooth behavior of the model indicates its capacity to provide mild extrapolations beyond the calibrated mass range without introducing significant biases.

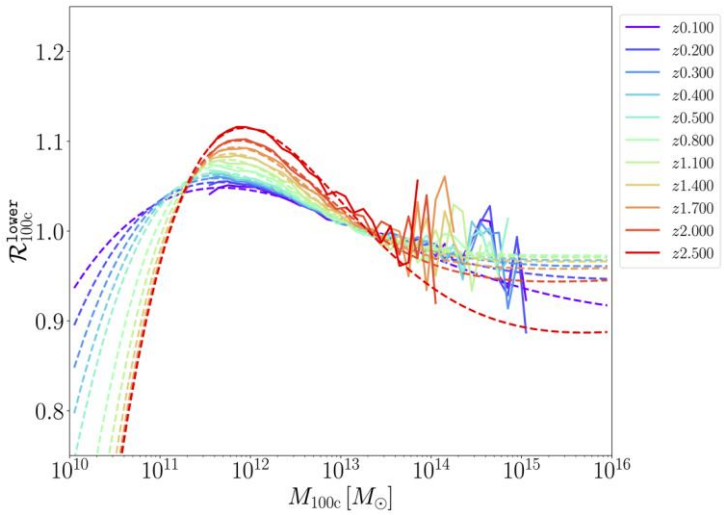

Figure 7. Resolution correction ratios under the lower scenario

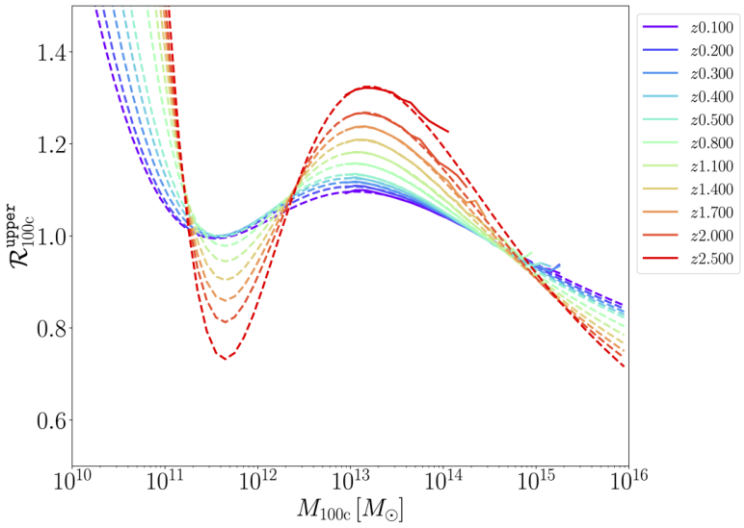

Figure 8. Resolution correction ratios under the upper scenario

We then apply our optimized resolution-correction model to the estimated HMFs, $\hat{n}(M,a)$. For halos measured in the low-resolution simulations, the correction must account for the two-step difference between low and high resolution. Accordingly, we apply the combined correction factor

$$\mathcal{R}_*(M,a) = \mathcal{R}_*^{\mathrm{lower}}(M,a) \cdot \mathcal{R}_*^{\mathrm{upper}}(M,a), \tag{34}$$

Where $\mathcal{R}_*^{\mathrm{upper}}$ converts low to base, and $\mathcal{R}_*^{\mathrm{lower}}$ further converts base to high. In contrast, for the base resolution simulations, only the single-step correction relative to the high-resolution case is required, so we adopt

$$\mathcal{R}_*(M,a) = \mathcal{R}_*^{\mathrm{lower}}(M,a). \tag{35}$$

This procedure ensures that all measured HMFs, regardless of their original particle resolution, are homogenized to the high resolution standard, thereby enabling a consistent calibration of the analytic HMF model.

3.5. Transformation to the dimensionless function

After correcting for resolution effects, we perform an additional transformation of the HMF into its dimensionless form. The motivation for this step stems from the fact that, as discussed earlier, the halo mass function $\hat{n}(M,a)$ is not itself the most natural quantity for theoretical modeling. The abundance of halos per unit volume and mass depends directly on the choice of halo mass definition and simulation setup, which complicates comparisons across cosmologies and redshifts. By contrast, expressing the HMF in terms of the dimensionless mass function provides a more universal quantity, which naturally arises in analytic theories such as Press–Schechter and excursion set formalisms, and is therefore better suited for theoretical predictions.

Accordingly, we translate the discrete HMF $\hat{n}(M,a)$ into its corresponding binned, dimensionless form $\hat{f}_{\mathrm{h}}(\hat{\mu}_{\mathrm{h}},a)$, defined as

$$\frac{\hat{n}(M,a)}{R_*(M,a)} = \hat{f}(\hat{\mu}_{\mathrm{h}},a)\frac{\bar{\rho}_{\mathrm{h}}}{M}\frac{\Delta\ln\hat{\mu}_{\mathrm{h}}}{\Delta\log_{10}M}, \tag{36}$$

Where the subscript h denotes the halo matter component, including CDM plus baryons, but excluding massive neutrinos. Since neutrinos have large thermal velocities and are unlikely to remain gravitationally bound within halos, we define

$$\bar{\rho}_{\mathrm{h}} = \bar{\rho}_{\mathrm{CDM}} + \bar{\rho}_{\mathrm{b}} = \bar{\rho}_{\mathrm{m}} - \bar{\rho}_{\nu}. \tag{37}$$

This definition is particularly useful for cosmologies including massive neutrinos, as it ensures a consistent treatment of halo mass relative to the clustering components. Accordingly, the formalism introduced in Section 2 can be rewritten in terms of halo matter components.

In this context, $\hat{\mu}_{\mathrm{h}}(M,a)$ denotes the simulated estimate of the halo peak height, defined as

$$\hat{\mu}_{\mathrm{h}}(M,a) = \frac{\delta_{\mathrm{c}}}{\hat{\sigma}_{\mathrm{h}}(M,a)}, \tag{38}$$

Where δ_{c} is the linear collapse threshold. In practice, numerical limitations introduce discrepancies between the simulated estimate $\hat{\mu}_{\mathrm{h}}$ and the theoretical value μ_{h}. The dominant source of this mismatch arises from the finite simulation volume: modes with wavelengths larger than the box size are absent, which leads to an underestimate of the halo mass variance $\hat{\sigma}_{\mathrm{h}}$ relative to the theoretical prediction σ_{h}. The suppression of large-scale power reduces the abundance of the most massive halos, effectively biasing the high-mass end of the HMF.

To account for this effect, we correct the variance using a volume factor $\sigma_{\mathrm{h}}(M_{\mathrm{v}},a)$, such that

$$\hat{\sigma}^2_{\mathrm{h}}(M,a) = \sigma^2_{\mathrm{h}}(M,a) - \sigma^2_{\mathrm{h}}(M_{\mathrm{v}},a), \tag{39}$$

With the effective volume mass defined as $M_{\mathrm{v}} = \bar{\rho}_{\mathrm{h}}\,L^3$. Here, $\sigma^2_{\mathrm{h}}(M,a)$ is the theoretical mass variance of the linear halo matter density field, calculated from the linear halo matter power spectrum $P^{\mathrm{L}}_{\mathrm{hh}}(k,a)$ via

$$\sigma^2_{\mathrm{h}}(M,a) = \int_0^\infty P^{\mathrm{L}}_{\mathrm{hh}}(k,a)\left|\widetilde{W}(kR_{\mathrm{h}})\right|^2\frac{k^2\,\mathrm{d}k}{2\pi^2}, \tag{40}$$

Where $\widetilde{W}(kR_{\rm h})$ is the Fourier transform of the spherical top-hat filter of radius

$$R_{\rm h} = \left(\frac{3M}{4\pi\bar{\rho}_{\rm h}}\right)^{1/3}, \tag{41}$$

Corresponding to the halo Lagrangian radius of mass M.

Given the extremely large volumes of the Abacus-Summit simulations ($L \gtrsim 1\,\mathrm{Gpc}$), the impact of this correction on the dimensionless mass function is very small ($\lesssim 0.5\%$). Nevertheless, we include it for completeness and consistency in our analysis.

After filtering out boundary halo mass bins with unreliable measurements, applying all systematic corrections, and performing the transformation, we finally obtain the dimensionless form of binned mass function $\hat{f}_{\rm h}(\hat{\mu}_{\rm h}, a)$. The resulting functions are shown in Fig.11 across all redshift snapshots and under different halo mass definitions. Compared to the original halo mass functions $\hat{n}(M, a)$, the dimensionless representation exhibits a much higher degree of universality, as expected from its construction, since it naturally accounts for the scaling with background density and linear variance. Nonetheless, the universality is not exact: residual dependencies on redshift and cosmology remain, reflecting both genuine physical effects – for instance, structure growth and collapse thresholds – and numerical limitations.

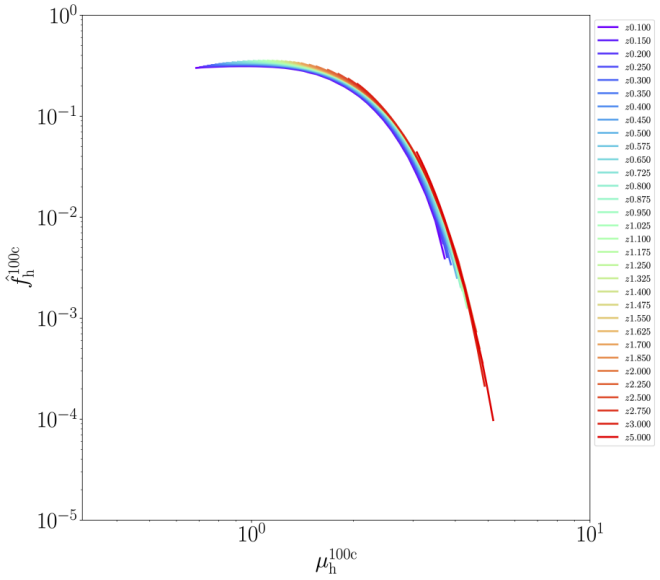

Figure 9. Dimensionless mass function $\hat{f}_{\rm h}$ from the Abacus-Summit simulations for all available redshift snapshots

In light of these properties, we adopt the dimensionless mass function as our key summary statistic. In the following section, we develop a parameterised analytic model, $f_{\rm h}(\hat{\mu}_{\rm h}, a \,|\, \boldsymbol{\theta})$, designed to capture the remaining redshift and cosmology dependence while retaining the improved universality of the transformed quantity. This provides a more robust theoretical framework for extrapolating beyond the simulation domain and for comparison with observational constraints.

4. Enhanced Analytic Modeling

This section introduces the novel analytic expression we develop to improve the precision of the HMF across a wide range of cosmological models. We then employ MCMC optimization to calibrate the best-fitting analytic form, and subsequently evaluate the performance of our modeling in comparison with existing results from the literature.

4.1. Mathematical expressions

A key limitation of standard fitting functions for the HMF is their restricted flexibility in modeling the complex, non-universal evolution across redshift and cosmology. To address this, we adopt the following parametric form:

$$\frac{f_{\rm h}(\hat{\mu}_{\rm h})}{\mathcal{F}} = (\zeta\,\hat{\mu}_{\rm h})^{\mathcal{A}}[1 + \mathcal{B}\,(\zeta\,\hat{\mu}_{\rm h})^{\mathcal{C}}]\exp[-\mathcal{D}\,(\zeta\,\hat{\mu}_{\rm h})^{\mathcal{E}}], \tag{42}$$

Where $\mathcal{A}, \mathcal{B}, \mathcal{C}, \mathcal{D}, \mathcal{E}, \mathcal{F}$, are free coefficients that depend explicitly on both redshift and cosmology for a given halo mass definition, unlike earlier formulae discussed in Section 2. Here, $\hat{\mu}_{\rm h}$ is the simulation-based estimate of the halo peak height, corrected for finite-volume effects as described in Section 3. This correction removes contributions from modes larger than the simulation box, thereby preventing a spurious suppression of the most massive halos, although the effect is small.

The prefactor ζ introduces additional redshift and cosmology dependence by accounting for variations in the critical overdensity $\delta_{\rm c}$.. We parameterize it as

$$\zeta = \left(1 + \alpha_\zeta\, a^{\beta_\zeta}\right) \cdot \left(1 + \gamma_\zeta\, \hat{\xi}_{\rm h}^{\kappa_\zeta}\right) \cdot \left(1 + \lambda_\zeta\, \hat{\eta}_{\rm h}\right), \tag{43}$$

Where $\alpha_\zeta, \beta_\zeta, \gamma_\zeta, \kappa_\zeta, \lambda_\zeta$ are free model coefficients. Here,

$$\hat{\xi}_{\rm h} = \left(\frac{{\rm dln}\hat{\mu}_{\rm h}}{{\rm dln}a}\right)_{\hat{\mu}_{\rm h}=1}, \tag{44}$$

Is the logarithmic derivative of the halo peak height with respect to the scale factor, analogous to the linear growth rate. In addition,

$$\hat{\eta}_{\rm h} = \left(\frac{{\rm dln}\hat{\mu}_{\rm h}}{{\rm dln}R_{\rm h}}\right)_{\hat{\mu}_{\rm h}=1}, \tag{45}$$

Is the logarithmic derivative of $\hat{\mu}_{\rm h}$ with respect to the halo Lagrangian radius, which traces the effective slope of the matter power spectrum.

Similarly, the coefficients $\mathcal{A}, \mathcal{B}, \mathcal{C}, \mathcal{D}, \mathcal{E}$ are allowed to vary with redshift and cosmology following an analogous form:

$$\begin{aligned}
\mathcal{A} &= \exp(\alpha_{\mathcal{A}}) \cdot a^{\beta_{\mathcal{A}}} \cdot (1 + \gamma_{\mathcal{A}}\, \xi^{\kappa_{\mathcal{A}}}) \cdot [1 + \lambda_{\mathcal{A}}\, \eta], \\
\mathcal{B} &= \exp(\alpha_{\mathcal{B}}) \cdot a^{\beta_{\mathcal{B}}} \cdot (1 + \gamma_{\mathcal{B}}\, \xi^{\kappa_{\mathcal{B}}}) \cdot [1 + \lambda_{\mathcal{B}}\, \eta], \\
\mathcal{C} &= \exp(\alpha_{\mathcal{C}}) \cdot a^{\beta_{\mathcal{C}}} \cdot (1 + \gamma_{\mathcal{C}}\, \xi^{\kappa_{\mathcal{C}}}) \cdot [1 + \lambda_{\mathcal{C}}\, \eta], \\
\mathcal{D} &= \exp(\alpha_{\mathcal{D}}) \cdot a^{\beta_{\mathcal{D}}} \cdot (1 + \gamma_{\mathcal{D}}\, \xi^{\kappa_{\mathcal{D}}}) \cdot [1 + \lambda_{\mathcal{D}}\, \eta], \\
\mathcal{E} &= \exp(\alpha_{\mathcal{E}}) \cdot a^{\beta_{\mathcal{E}}} \cdot (1 + \gamma_{\mathcal{E}}\, \xi^{\kappa_{\mathcal{E}}}) \cdot [1 + \lambda_{\mathcal{E}}\, \eta].
\end{aligned} \tag{46}$$

Finally, the coefficient $\mathcal{F}$ is fixed by a normalization condition that enforces mass conservation. Specifically, the total mass density in halos must equal the mean matter density of the universe, $bar\rho_{\rm h}$

$$\int_0^\infty M\, \frac{{\rm d}n}{{\rm dlog}_{10}M}\, {\rm dlog}_{10}M = \bar{\rho}_{\rm h} \int_0^\infty f_{\rm h}\,(\mu)\, {\rm dln}\mu. \tag{47}$$

Since the left-hand side integrates to $\bar{\rho}_{\rm h}$, the multiplicity function must satisfy

$$\int_0^\infty f\,(\mu)\,\mathrm{d}\ln\mu = 1. \tag{48}$$

This yields the normalization factor $\mathcal{F}$

$$\mathcal{F} = \frac{\mathcal{D}^{\frac{\mathcal{A}+\mathcal{C}}{\mathcal{E}}}\mathcal{E}}{\mathcal{D}^{\frac{\mathcal{C}}{\mathcal{E}}}\Gamma\left(\frac{\mathcal{A}}{\mathcal{E}}\right)+\mathcal{B}^{\mathcal{C}}\,\Gamma\left(\frac{\mathcal{A}+\mathcal{C}}{\mathcal{E}}\right)} \tag{49}$$

In total, this formulation introduces 30 free parameters, $\boldsymbol{\theta}$, analogous to the parameterization used for the resolution correction model. We calibrate these parameters using MCMC. For simplicity, we adopt flat priors for each parameter:

$$\mathcal{P}(\boldsymbol{\theta}) \sim \mathcal{U}(-5, +5), \tag{50}$$

And assume a Gaussian likelihood,

$$\mathcal{L} = \ln\mathcal{P}\left(\hat{\mathbf{f}} \mid \boldsymbol{\theta}\right) = -\frac{1}{2}\ln\left[(2\pi)^{\mathcal{N}_f}\,|\boldsymbol{\Sigma}_\mathbf{f}|\right] - \frac{1}{2}\left[\hat{\mathbf{f}} - \mathbf{f}(\boldsymbol{\theta})\right]^\dagger \boldsymbol{\Sigma}_\mathbf{f}{}^{-1}\left[\hat{\mathbf{f}} - \mathbf{f}(\boldsymbol{\theta})\right], \tag{51}$$

Where $\hat{\mathbf{f}}$ are the simulation measurements, $\mathbf{f}(\boldsymbol{\theta})$ are model predictions under parameter $\boldsymbol{\theta}$, $\mathcal{N}_f$ is the number of data points, and $\boldsymbol{\Sigma}_\mathbf{f}$ is the covariance matrix. At leading order we adopt diagonal Poisson uncertainties and neglect cross-covariances, as justified earlier.

The optimization is performed using the emcee, with 4096 walkers and 4096 steps. We discard the first 50% of the chains as burn-in and adopt the maximum-posterior point $\boldsymbol{\theta}_* = \mathrm{argmax}\left[\mathcal{P}\left(\boldsymbol{\theta} \mid \hat{\mathbf{f}}\right)\right]$ as the best-fitting parameter set. The results are reported in Tab. 3 for different halo mass definitions.

Table 3. Best-fitting parameters obtained from the MCMC optimization of the HMF model, $f_\mathrm{h}(\mu)$, for six SO definitions: $100\mathrm{c}$, $200\mathrm{c}$, $200\mathrm{m}$, $500\mathrm{c}$, $1000\mathrm{c}$, and Virial.

θ	100c	200c	200m	500c	1000c	virial
α_ζ	-0.1052	-0.3500	-0.2289	-0.0158	0.0857	-0.2019
β_ζ	0.3148	0.5573	0.4177	0.4904	-0.6927	0.3806
γ_ζ	-0.0391	0.0642	0.1803	-0.1593	-0.3837	0.0514
κ_ζ	-0.7552	0.3290	-0.9829	0.3192	0.0940	0.2544
λ_ζ	0.4805	0.5337	0.1902	0.4227	-0.2843	0.1176
$\alpha_\mathcal{A}$	-1.8159	-1.8504	-2.0124	-3.1498	-2.4656	-1.7835
$\beta_\mathcal{A}$	-0.4383	-0.2837	-0.3935	-0.4997	-0.1731	-0.4060
$\gamma_\mathcal{A}$	1.3380	1.1751	1.2829	2.2102	0.8385	0.8023
$\kappa_\mathcal{A}$	0.8634	1.0053	-0.8747	0.0168	0.7227	0.0262
$\lambda_\mathcal{A}$	0.5358	0.3769	0.2913	0.4135	0.0454	0.4588
$\alpha_\mathcal{B}$	-0.3733	-1.4667	1.0526	-1.4655	-0.4036	1.2684
$\beta_\mathcal{B}$	0.1216	1.4845	2.6266	1.1542	1.1376	2.4097
$\gamma_\mathcal{B}$	3.7941	1.6671	0.1987	2.8054	0.2524	0.9029
$\kappa_\mathcal{B}$	3.5268	2.4607	3.8552	1.8081	-1.8424	2.9879
$\lambda_\mathcal{B}$	1.1101	2.9370	3.4577	3.8080	3.9965	-0.2744
$\alpha_\mathcal{C}$	-1.2471	-2.3611	-3.1826	-0.7233	-0.5346	-2.6356
$\beta_\mathcal{C}$	2.6401	1.8767	1.2604	0.5125	0.7326	1.0539

θ	100c	200c	200m	500c	1000c	virial
$\gamma_{\mathcal{C}}$	1.3032	1.8610	3.8705	0.8019	2.7986	1.4532
$\kappa_{\mathcal{C}}$	3.5845	2.3659	2.5003	1.8914	-0.1119	2.8308
$\lambda_{\mathcal{C}}$	-0.3730	1.1433	0.3983	0.2712	-0.8496	1.2803
$\alpha_{\mathcal{D}}$	-1.6292	-1.2570	-2.5534	-1.9981	-0.6356	-1.5845
$\beta_{\mathcal{D}}$	-0.1578	0.1285	-0.2322	-0.1825	0.3584	-0.1392
$\gamma_{\mathcal{D}}$	0.7170	0.5148	1.6947	1.0743	0.8118	0.3628
$\kappa_{\mathcal{D}}$	3.0537	3.9654	0.1940	0.3633	-0.9629	2.7705
$\lambda_{\mathcal{D}}$	0.1323	-0.2733	0.2142	0.3886	1.2240	0.7360
$\alpha_{\mathcal{E}}$	-0.1318	-0.2553	-0.0515	0.0690	-0.1887	0.0353
$\beta_{\mathcal{E}}$	0.0250	0.0058	0.0877	0.0685	0.0212	0.0508
$\gamma_{\mathcal{E}}$	1.4073	1.7923	1.5220	1.3666	1.5612	1.2393
$\kappa_{\mathcal{E}}$	-0.6204	-0.8242	0.1134	-0.3028	0.4276	-0.4988
$\lambda_{\mathcal{E}}$	-0.2717	-0.1360	-0.1257	-0.2345	0.3180	-0.2359

4.2. Performance of modeling

Our analytic model achieves percent-level precision in reproducing the HMF across a wide range of halo masses and redshifts. As illustrated in Fig. 10, the agreement between the model predictions and the Abacus-Summit simulation measurements remains remarkably tight, with typical deviations confined to the $2-3\%$ level over the mass interval $10^{11}\,M_{\odot} \lesssim M \lesssim 10^{15}\,M_{\odot}$. This performance persists across redshifts from $z = 0.01$ up to $z = 3.00$, demonstrating that the extended parameterization introduced in this work successfully captures the non-universal evolution of the HMF with redshift. Importantly, our model does not require ad hoc redshift-dependent corrections, but instead incorporates cosmology- and redshift-sensitive terms directly into the functional form, thereby yielding a more physically motivated description.

Our model demonstrates clear improvements over existing HMF fitting formulae, which typically achieve $\sim 5-10\%$ accuracy but show systematic deviations at low masses ($M \lesssim 10^{12} M_{\odot}$) or high masses ($M \gtrsim 10^{14} M_{\odot}$), particularly at higher redshifts. In contrast, our analytic expression maintains consistent accuracy across the full dynamic range, with residuals staying within the 5% tolerance band. The model's robustness extends beyond ΛCDM, as its cosmology-dependent terms preserve $\lesssim 5\%$ accuracy for non-standard scenarios including massive neutrinos, modified power spectra, and evolving dark energy equations of state, making it suitable for both standard and beyond-standard-model cosmological studies.

In summary, the analytic model developed here represents a significant improvement in precision and generality for HMF predictions. It achieves near-universal performance across halo masses, redshifts, and cosmologies, making it well-suited for upcoming large-scale structure surveys that demand sub-percent-level accuracy in the modeling of halo abundances. The combination of percent-level agreement with simulations, improved consistency relative to existing formulae, and demonstrated applicability to non-ΛCDM scenarios highlights the strength of our approach as a new standard for analytic HMF modeling.

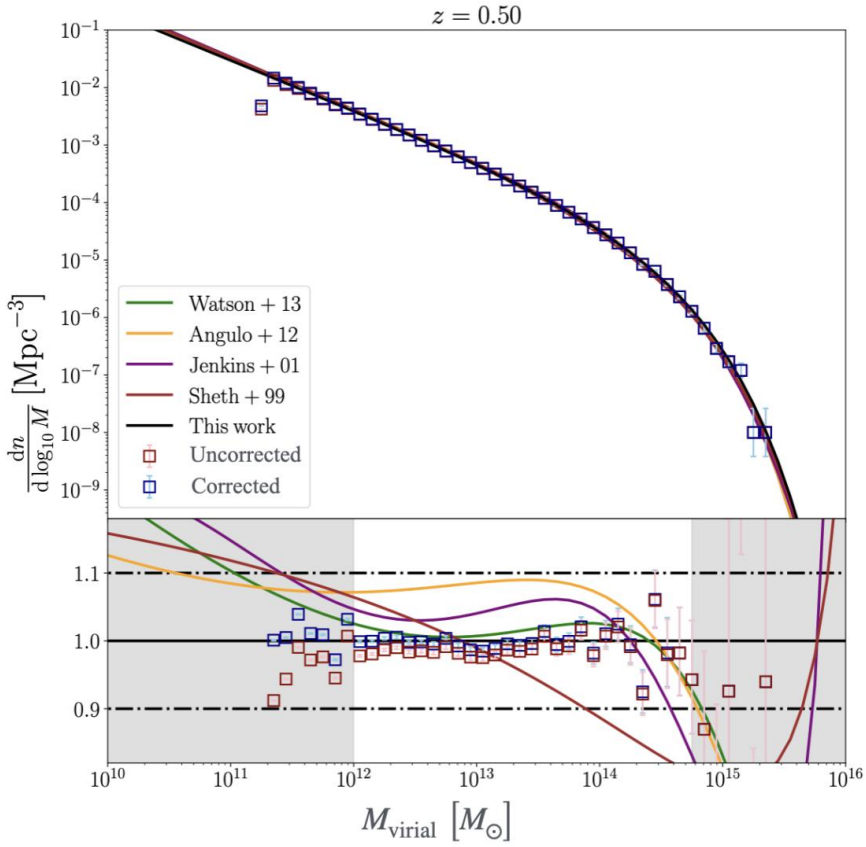

Figure 10. Performance of our analytic modeling of the virial HMF

5. Discussions

5.1. Advancements of this work

This work advances HMF modeling through two key innovations. First, we leverage the unprecedented statistical power of the Abacus-Summit simulation suite, combining large volumes ($2\ \mathrm{Gpc}/h$) with high resolution ($2 \times 10^9 M_\odot/h$) across 97 cosmologies, including extensions beyond ΛCDM. Multiple realizations enable robust variance estimation, while varied volumes/resolutions quantify systematics - uniquely supporting HMF calibration from 10^{11} to $10^{15} M_\odot$ across redshifts $0 < z < 30$. Second, we develop a physically-motivated analytic framework using cosmology-dependent variables (peak height, scaling factors, and their derivatives) rather than direct parameter interpolation. This approach maintains $< 5\%$ accuracy even when extrapolated beyond the training domain, outperforming machine-learning emulators that require costly retraining for new physics.

Our model's physics-based formulation provides several advantages over data-driven approaches. By encoding cosmology dependence through structure growth variables, it naturally adapts to modified gravity, interacting dark matter, or dynamical dark energy without retraining - unlike emulators that suffer from the curse of dimensionality when expanding parameter spaces. The analytic form ensures numerical stability during extrapolation while capturing redshift evolution often missed in traditional fits. This combination of first-principles modeling with state-of-the-art simulations yields a versatile HMF applicable to both current analyses and future beyond-ΛCDM studies.

5.2. Current limitations and prospects

Our analytic HMF model achieves $2-3\%$ accuracy across a wide dynamic range in mass and redshift, slightly less precise than simulation-based emulators but significantly more versatile. While precision degrades to $\lesssim 5\%$ at high redshifts ($z \gtrsim 2$) and for non-ΛCDM cosmologies, the model maintains advantages of interpretability and broad applicability without requiring retraining for new

physics. This represents a practical trade-off between physical transparency and ultimate numerical precision.

Future improvements could incorporate symbolic regression to optimize the functional form and parameters, potentially enhancing accuracy while preserving interpretability. Additionally, systematic comparisons across different halo finders (e.g., FoF, ROCKSTAR) are needed to quantify $\sim 20\%$ variations in HMF amplitudes and assess their cosmological dependence, which could inform potential corrections for cross-survey consistency.

6. Summary and Conclusions

We present an enhanced analytic halo mass function (HMF) model achieving $2-3\%$ accuracy for ΛCDM cosmologies ($\lesssim 5\%$ for extensions) across $10^{11}-10^{15}M_{\odot}$ and $0<z<3$. The model incorporates redshift and cosmology dependence through physically motivated variables (μ, ξ, η), calibrated using the state-of-the-art Abacus-Summit simulations. This framework provides a robust, interpretable alternative to simulation-based emulators, particularly valuable for beyond-ΛCDM studies where emulators require costly retraining.

Our results demonstrate the viability of analytic approaches in the era of precision cosmology, with accuracy sufficient for upcoming surveys like Rubin and Euclid. Future improvements through symbolic regression and systematic halo-finder comparisons will further enhance the model's precision and applicability to next-generation cosmological analyses.

Acknowledgements

This is the place to fill in information about funds, sponsors, etc. that need to be thanked.

References

[1] Weinberg, S. 1972, 688.

[2] Smoot, G. F., Bennett, C. L., Kogut, A., et al. 1992, Astrophysical Journal Letters, 396, L1. doi:10.1086/186504.

[3] Bennett, C. L., Halpern, M., Hinshaw, G., et al. 2003, Astrophysical Journal Supplement Series, 148, 1, 1. doi:10.1086/377253.

[4] Pang, Y.-H., Zhang, X., & Huang, Q.-G. 2025, Journal of Cosmology and Astroparticle Physics, 2025, 4, 057. doi: 10.1088/1475-7516/2025/04/057.

[5] Kushnir, D. & Sharon, A. 2025, Monthly Notices of the Royal Astronomical Society, 538, 4, 2838. doi: 10.1093/mnras/staf431.

[6] DESI Collaboration, Abdul-Karim, M., Aguilar, J., et al. 2025, arXiv: 2503.14738. doi: 10.48550/arXiv.2503.14738

[7] Wright, A. H., Kuijken, K., Hildebrandt, H., et al. 2024, Astronomy & Astrophysics, 686, A170. doi: 10.1051/0004-6361/202346730.

[8] Bechtol, K., Sevilla-Noarbe, I., Drlica-Wagner, A., et al. 2025, arXiv: 2501.05739. doi: 10.48550/arXiv.2501.05739.

[9] Wright, A. H., Stölzner, B., Asgari, M., et al. 2025, arXiv: 2503.19441. doi: 10.48550/arXiv.2503.19441.

[10] Norman, M. L. 2010, arXiv: 1005.1100. doi: 10.48550/arXiv.1005.1100.

[11] Kravtsov, A. V. & Borgani, S. 2012, Annual Review of Astronomy and Astrophysics, 50, 353. doi: 10.1146/annurev-astro-081811-125502.

[12] Vikhlinin, A., Kravtsov, A. V., Burenin, R. A., et al. 2009, Astrophysical Journal, 692, 2, 1060. doi: 10.1088/0004-637X/692/2/1060.

[13] Umetsu, K. 2020, Astronomy and Astrophysics Review, 28, 1, 7. doi: 10.1007/s00159-020-00129-w.

[14] Ansarifard, S., Rasia, E., Biffi, V., et al. 2020, Astronomy & Astrophysics, 634, A113. doi: 10.1051/0004-6361/201936742.

[15] Carlstrom, J. E., Holder, G. P., & Reese, E. D. 2002, Annual Review of Astronomy and Astrophysics, 40, 643. doi: 10.1146/annurev.astro.40.060401.093803.

[16] Voit, G. M. 2005, Reviews of Modern Physics, 77, 1, 207. doi: 10.1103/RevModPhys.77.207.

[17] Bocquet, S., Dietrich, J. P., Schrabback, T., et al. 2019, Astrophysical Journal, 878, 1, 55. doi: 10.3847/1538-4357/ab1f10.

[18] Laureijs, R., Amiaux, J., Arduini, S., et al. 2011, arXiv: 1110.3193. doi: 10.48550/arXiv.1110.3193.

[19] Costanzi, M., Villaescusa-Navarro, F., Viel, M., et al. 2013, Journal of Cosmology and Astroparticle Physics, 2013, 12, 012. doi: 10.1088/1475-7516/2013/12/012.

[20] Villaescusa-Navarro, F., Hahn, C., Massara, E., et al. 2020, Astrophysical Journal Supplement Series, 250, 1, 2. doi: 10.3847/1538-4365/ab9d82.

[21] Garrison, L. H., Eisenstein, D. J., Ferrer, D., et al. 2021, Monthly Notices of the Royal Astronomical Society, 508, 1, 575. doi: 10.1093/mnras/stab2482.

[22] Heitmann, K., Bingham, D., Lawrence, E., et al. 2016, Astrophysical Journal, 820, 2, 108. doi: 10.3847/0004-637X/820/2/108.

[23] Nishimichi, T., Takada, M., Takahashi, R., et al. 2019, Astrophysical Journal, 884, 1, 29. doi: 10.3847/1538-4357/ab3719.